Reduced volume and reflection for bright optical tweezers with radial Laguerre–Gauss beams

J.-B. Béguin[a], J. Laurat[b], X. Luan[a], A. P. Burgers[a,1], Z. Qin[a,c], and H. J. Kimble[a,2]

[a]Norman Bridge Laboratory of Physics, California Institute of Technology, Pasadena, CA 91125; [b]Laboratoire Kastler Brossel, Sorbonne Université, CNRS, ENS-Université PSL, Collège de France, 75005 Paris, France; and [c]State Key Laboratory of Quantum Optics and Quantum Optics Devices, Institute of Opto-Electronics, Shanxi University, Taiyuan 030006, China

Contributed by H. J. Kimble, August 17, 2020 (sent for review July 6, 2020; reviewed by Takao Aoki and Mark Saffman)

Spatially structured light has opened a wide range of opportunities for enhanced imaging as well as optical manipulation and particle confinement. Here, we show that phase-coherent illumination with superpositions of radial Laguerre–Gauss (LG) beams provides improved localization for bright optical tweezer traps, with narrowed radial and axial intensity distributions. Further, the Gouy phase shifts for sums of tightly focused radial LG fields can be exploited for phase-contrast strategies at the wavelength scale. One example developed here is the suppression of interference fringes from reflection near nanodielectric surfaces, with the promise of improved cold-atom delivery and manipulation.

optical tweezer | Gouy phase | cold atoms | Laguerre–Gauss beams

Structuring of light has provided advanced capabilities in a variety of research fields and technologies, ranging from microscopy to particle manipulation (1–4). Coherent control of the amplitude, phase, and polarization degrees of freedom for light enables the creation of engineered intensity patterns and tailored optical forces. In this context, Laguerre–Gauss (LG) beams have been extensively studied. Among other realizations, tight focusing with subwavelength features was obtained with radially polarized beams (5, 6), as well as with opposite orbital angular momentum for copropagating fields (7). LG beams have also attracted interest for designing novel optical tweezers (8–10). Following the initial demonstration of an LG-based trap for neutral atoms (11), various configurations have been explored, including three-dimensional (3D) geometries with "dark" internal volumes (12–15) for atom trapping with blue-detuned light (16, 17).

For these and other applications of structured light, high spatial resolution is of paramount importance. However, in most schemes, resolution transverse to the optic axis largely exceeds that along the optic axis. For example, a typical bright optical tweezer formed from a Gaussian beam with wavelength $\lambda = 1\,\mu$m focused in vacuum to waist $w_0 = 1\,\mu$m has transverse confinement w_0 roughly three times smaller than its longitudinal confinement set by the Rayleigh range $z_R = \pi w_0^2/\lambda$. One way to obtain enhanced axial resolution is known as 4π microscopy (18, 19), for which counterpropagating beams form a standing wave with axial spatial scale of $\lambda/2$ over the range of z_R. However, 4π microscopy requires interferometric stability and delicate mode matching. Another method relies on copropagating beams each with distinct Gouy phases (20–22), which was proposed and realized mostly in the context of dark (i.e., blue-detuned) optical traps, either with two Gaussian beams of different waists or offset foci (23, 24) or with LG modes of different orders (14, 25). However, for bright (i.e., red-detuned) trap configurations, a comparable strategy has remained elusive.

In this article, we show that superpositions of purely radial LG modes can lead to reduced volume for bright optical traps. We also provide a scheme for implementation by way of a spatial light modulator (SLM) for beam shaping extended beyond the paraxial approximation into a regime of wavelength-scale traps. Significantly, apart from reduced trap volume, our study highlights differential Gouy phase shifts at the wavelength scale as a tool for imaging. An application is the strong suppression of interference fringes from reflections of optical tweezers near surfaces of nanophotonic structures, thereby providing a tool to integrate cold-atom transport and nanoscale quantum optics, a timely topic of paramount importance for the development of the waveguide quantum electrodynamics (QED) research field (26).

LG Superpositions in the Paraxial Limit

To gain an intuitive understanding, we first consider superpositions of LG modes within the familiar paraxial approximation. The positive frequency components of the electric field are denoted by $\vec{E}_{p,i} = \vec{x}u_p(x, y, z; w_i)e^{-ikz}$ with x-oriented linear polarization and propagation directed toward negative z values with longitudinal wave vector $k > 0$. The cylindrically symmetric complex scalar amplitude u_p for LG beams is as in refs. 27 and 28 and given explicitly in *SI Appendix*. The parameter w_i denotes the waist (i.e., $1/e^2$ intensity radius at $z = 0$ for a $p = 0$ Gaussian beam). The azimuthal mode number l is dropped with $l = 0$ throughout (i.e., pure radial LG beams with radial number p). For a given optical frequency, the phase of the field relative to that of a plane wave propagating along $-z$ [i.e., the Gouy phase (20–22)] is given by $\Psi_p(z) = \arg(\vec{E}_{p,i} \cdot \vec{x}e^{ikz}) = (2p + 1)\arctan(z/z_{R,i})$, with the Rayleigh range $z_{R,i} = \pi w_i^2/\lambda$.

Although we have analyzed diverse superpositions of radial LG modes, for clarity we confine our discussion here to the particular superposition $\vec{E}_\Sigma = \vec{E}_0 + \vec{E}_2 + \vec{E}_4$ due to its improvement in atom delivery. For example, the coherent superposition

Significance

Nanoscale dielectric devices are capable of mediating long-range atom–atom interactions using guided mode photons, as well as long-range photon–photon interactions mediated by lattices of atoms. Such systems have the potential to provide new tools for quantum science. However, an outstanding challenge is the delivery of single atoms to optical traps near nanophotonic devices. We introduce a capability that could increase fidelity for atom-lattice assembly near nanophotonic structures. Other applications include imaging strategies.

Author contributions: J.-B.B., J.L., X.L., A.P.B., Z.Q., and H.J.K. designed research; J.-B.B., J.L., X.L., A.P.B., Z.Q., and H.J.K. performed research; J.-B.B., J.L., and X.L. contributed new analytic tools; J.-B.B., J.L., and X.L. analyzed data; and J.-B.B., J.L., X.L., A.P.B., Z.Q., and H.J.K. wrote the paper.

Reviewers: T.A., Waseda University; and M.S., University of Wisconsin–Madison.

The authors declare no competing interest.

[1]Present address: Department of Electrical Engineering, Princeton University, Princeton, NJ 08540.

[2]To whom correspondence may be addressed. Email: hjkimble@caltech.edu.

This article contains supporting information online at https://www.pnas.org/lookup/suppl/doi:10.1073/pnas.2014017117/-/DCSupplemental.

First published October 2, 2020.

$\vec{E}_0 + \vec{E}_6$ gives a narrower axial focal width as compared with that of $\vec{E}_0 + \vec{E}_2 + \vec{E}_4$. However, this comes at the price of strong axial side lobes, which are a hindrance for the presented atom delivery scheme due to significant revivals of reflection fringing. For the sole purpose of free-space trapping, note that the phase modulation strategy illustrated in this work is deterministic. Cold atoms initially loaded into a conventional $p = 0$ optical tweezer can be transfered to an LG beam tweezer by progressively turning on other p-mode components.

Fig. 1 *A* and *B* provides the calculated intensity distributions for the fundamental Gaussian mode $\vec{E}_0$ (blue) and for the superposition (orange) along the x axis in the focal plane and along the z propagation axis, respectively. As shown by the line cuts and *Insets* in Fig. 1 *A* and *B*, there is a large reduction in focal volume V_Σ for $|\vec{E}_\Sigma|^2$ relative to V_0 for $|\vec{E}_0|^2$. Here, $V = \Delta x \Delta y \Delta z$, with $\Delta x, \Delta y, \Delta z$ taken to be the full widths at half maxima for the intensity distributions along x, y, z in Fig. 1 *A* and *B*, leading to $V_0/V_\Sigma \simeq 22$ where $V_0 = 8.6\ \mu\text{m}^3$ and $V_\Sigma = 0.39\ \mu\text{m}^3$ as detailed in *SI Appendix*.

Recall that the rms radial size σ_p of the beam intensity increases as $\sigma_p = w_i\sqrt{2p+1}$ (29), associated with the LG basis scale parameter w_i (i.e., fixed Rayleigh range). This leads to a larger divergence angle for higher radial number p. Therefore, transverse clipping and the impact of diffraction effects due to the constraints of finite aperture stop sizes in any realistic imaging lens system (e.g., finite lens numerical aperture (NA), pupil radius) need to be included and are thus analyzed further below.

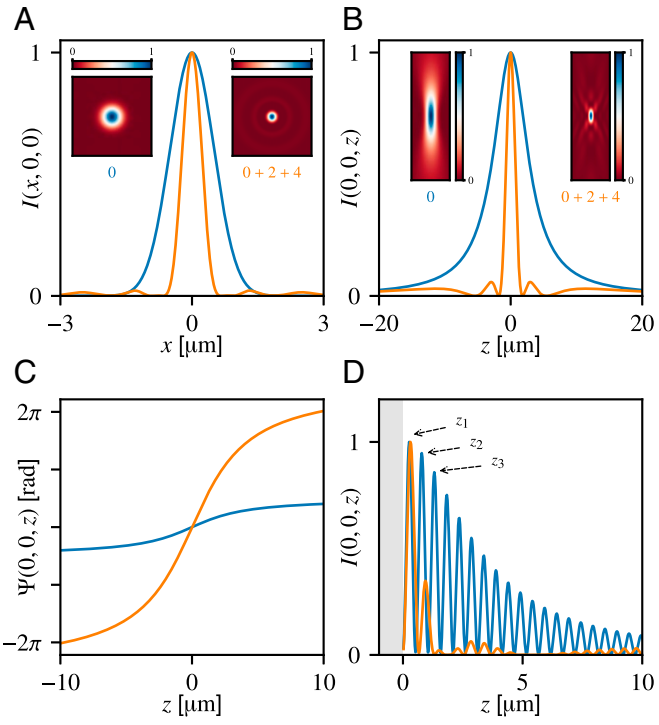

Fig. 1. Comparison between the fundamental Gaussian mode $\vec{E}_0$ (blue) and the superposition of radial p modes $\vec{E}_\Sigma$ (orange) with $p = 0, 2, 4$. The plots are calculated for the paraxial case, with $w_0 = 1\ \mu$m and $\lambda = 1\ \mu$m. (*A*) x-line cut transverse intensity profiles. *Insets* provide the x–y distribution in the focal plane. (*B*) z-line cut axial intensity profiles. *Insets* correspond to the x–z distribution in the $y = 0$ plane. (*C*) Gouy phases Ψ_0 (blue) for $\vec{E}_0$ and Ψ_Σ (orange) for $\vec{E}_\Sigma$ along the optical axis z. (*D*) Reflection fringes due to a semi-infinite planar surface (gray), with amplitude reflection coefficient $r = -0.8$ and focus at the surface $z = 0$. z_i indicate successive maxima. All intensities are normalized to their peak values in *A*, *B*, and *D*.

Also relevant is that individual u_p modes have identical spatial profiles $|u_p(0,0,z)|$ along z. The reduced spatial scale for the superposition $\vec{E}_\Sigma$ results from the set of phases $\{\Psi_p(z)\}$ for $p = 0, 2, 4$, with Gouy phases for the total fields $\vec{E}_0$ and $\vec{E}_\Sigma$ shown in Fig. 1*C*. The Gouy phase for $\vec{E}_\Sigma$ also leads to suppressed interference fringes in regions near dielectric boundaries as shown in Fig. 1*D*.

Beyond volume, a second metric for confinement in an optical tweezer is the set of oscillation frequencies for atoms trapped in the tweezer's optical potential. Trap frequencies for cesium (Cs) atoms localized within tweezers formed from $\vec{E}_0$ and $\vec{E}_\Sigma$ as in Fig. 1 *A* and *B* are presented in *SI Appendix*, with significant increases for $\vec{E}_\Sigma$ as compared with $\vec{E}_0$. The values for trap volume and frequency are provided later with the full model.

Field Superpositions Generated with an SLM

Various methods have been investigated to produce LG beams with high purity (30). A relatively simple technique consists of spatial phase modulation of a readily available Gaussian source beam with a series of concentric circular two-level phase steps to replicate the phase distribution of the targeted field $\vec{E}_{p_{target}}$ with $p_{target} > 0$ (31). The maximum purity for this technique is ~ 0.8, with the deficit of ~ 0.2 due to the creation of p components other than the single p_{target}. Moreover, it is desirable to generate not only high-purity LG beams for a single p_{target} but also, arbitrary coherent sums of such modes, as for $\vec{E}_\Sigma$. Rather than generate separately each component from the set of required radial modes $\{p\}_{target}$, here we propose a technique with a single SLM that eliminates the need to coherently combine multiple beams for the set $\{p\}_{target}$. Our strategy reproduces simultaneously both the phase and the amplitude spatial distribution of the desired complex electric field (and in principle, the polarization distribution for propagation phenomena beyond the scalar field approximation).

Fig. 2 shows numerical results for a Gaussian source field $\vec{E}_s$ input to an SLM to create the field $\vec{E}_i$ leaving the SLM. $\vec{E}_i$ is then focused by an ideal thin spherical lens and propagated to the focal plane at $z = 0$ by way of the Fresnel–Kirchhoff scalar diffraction integral.

Fig. 2*A* illustrates our technique for the case of the target field $\vec{E}_\Sigma$. Amplitude information for the sum of complex fields comprising $\vec{E}_\Sigma$ is encoded in a phase mask by contouring the phase modulation depth of a superimposed blazed grating as developed in refs. 32 and 33. For atom trapping applications with scalar polarizability, the tweezer trap depth is proportional to the peak optical intensity in the focal plane, where for the coherent field superposition $\vec{E}_\Sigma$, the peak intensity reaches a value identical to that for $\vec{E}_0$ at $1/3$ of the invested trap light power, which helps to mitigate losses associated with the blazed grating. We remark that it is not crucial to convert from $\vec{E}_0$ with simultaneous amplitude and phase modulation strategies (e.g., consider flat-top beams) (30).

The resulting intensity distributions in the focal plane are plotted in Fig. 2 *B* and *C* (red solid) for comparison with the ideal $\vec{E}_i = \vec{E}_0$ (gray solid) and ideal $\vec{E}_i = \vec{E}_\Sigma$ (black dashed). These results are encouraging for our efforts to experimentally generate tightly focused radial LG superpositions (*SI Appendix* has initial laboratory results).

Vector Theory of LG Superpositions

Figs. 1 and 2 provide a readily accessible understanding of focused LG mode superpositions within the paraxial approximation. To obtain a more accurate description for tight focusing on a wavelength scale, we next consider a vector theory. Using the vectorial Debye approximation (34, 35) and an input field

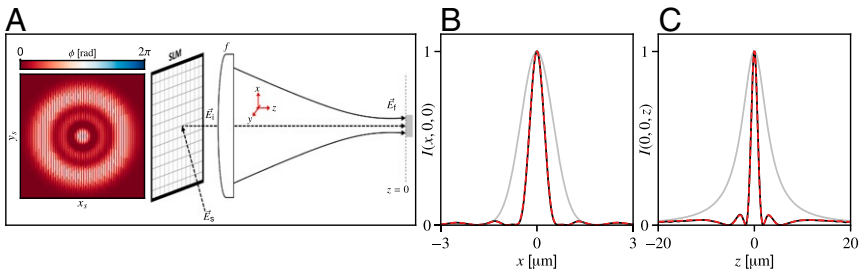

Fig. 2. (*A*, *Left*) Calculated transverse phase profile ϕ applied to the SLM to generate the field $\vec{E}_\Sigma$. (*A*, *Right*) An incident Gaussian source field $\vec{E}_s$ is incident on the SLM. The first-order diffracted field $\vec{E}_i$ on the exit plane of the SLM is then focused by an objective lens with effective focal length f to form the field $\vec{E}_f$ in the focal plane at $z=0$. (*B*) Line cuts along x of $|\vec{E}_f|^2$ in the focal plane for modulation of the SLM with $\phi(x_s, y_s)$ calculated to generate $\vec{E}_\Sigma$ (red solid line), ideal target intensity $|\vec{E}_\Sigma|^2$ (black dashed line), and Gaussian intensity $|\vec{E}_0|^2$ (gray line). (*C*) As in *B* but for line cuts along z with $x=y=0$.

$\vec{E}_0$ with waist $w_0 \gg \lambda$ and polarization aligned along the x axis, we calculate the field distribution at the output of an aplanatic objective with fixed $\mathrm{NA}=\sin\theta_{\max}$.*

By convention, the ratio of input waist $w_{0,\mathrm{in}}$ to the pupil radius R_p is called the filling factor $F_0 \equiv \frac{w_{0,\mathrm{in}}}{R_p}$, where $R_p = f\times\mathrm{NA}$ for focal length f. F_0 is an important parameter for focusing LG beams at finite aperture, and different filling factors may have very different beam shapes. The curves in Fig. 3 are calculated numerically using the Debye–Wolf vector theory for filling factors $F_0=0.35$ and $F_0=0.45$, each with fixed numerical aperture $\mathrm{NA}=0.7$. These parameters provide $1/e^2$ intensity radii $w_{e2}=\{1.3, 1.0\}$ μm in the focal plane with the input $\vec{E}_0$ for $F_0=\{0.35, 0.45\}$, respectively.

For $p=0$ and $F_0=0.35$, the intensity profiles in both radial and axial directions in the focal plane (violet curves in Fig. 3 *A* and *B*) are quite similar to those in Fig. 1 *A* and *B*. Likewise, for input of the "0 + 2 + 4" superposition at the same filling factor $F_0=0.35$ (brown curves in Fig. 3 *A* and *B*), the intensity profiles are again similar to Fig. 1 *A* and *B* and evidence reductions in both transverse and longitudinal widths relative to the $p=0$ input even in the vector theory with wavelength-scale focusing.

More quantitatively, with $F_0=0.35$ the full width at half maximums (FWHMs) for the $\vec{E}_\Sigma$ input are $\Delta x_\Sigma = 0.84\,\mu\mathrm{m}$, $\Delta y_\Sigma = 0.72\,\mu\mathrm{m}$, and $\Delta z_\Sigma = 2.78\,\mu\mathrm{m}$, corresponding to a focal volume $V_\Sigma = 1.7\,\mu\mathrm{m}^3$ for the central peak. For the $p=0$ input with $F_0=0.35$, the FWHMs of the central peaks for each direction are $\Delta x_0 = 1.55\,\mu\mathrm{m}$, $\Delta y_0 = 1.51\,\mu\mathrm{m}$, and $\Delta z_0 = 10.3\,\mu\mathrm{m}$, corresponding to a focal volume $V_0 = 24\,\mu\mathrm{m}^3$. The latter reduces to $V_0 = 5.62\,\mu\mathrm{m}^3$ under transverse clipping with $F_0=1$ (*Optimal Filling Factors*). The ratio of focal volumes defined via FWHMs for inputs with $p=0$ and the $\vec{E}_\Sigma$ superposition is then $V_0/V_\Sigma \simeq 14$. Moreover, for red-detuned optical traps associated with the line cuts in Fig. 3 *A* and *B*, we find trap frequencies for input $\vec{E}_\Sigma$ to be $\omega_x^\Sigma = 2\pi\times 124\,\mathrm{kHz}$ and $\omega_z^\Sigma = 2\pi\times 33\,\mathrm{kHz}$.

However, increasing of the filling factor beyond $F_0=0.35$ for the 0 + 2 + 4 superposition input does not lead to increases in trap frequencies nor further reductions of the focal volume. As shown by the brown curves in Fig. 3 *C* and *D* for filling factor $F_0=0.45$, the central width of the focus is not reduced; rather, the peak of two side lopes increases. This is not the case for the $p=0$ input (violet curves in Fig. 3 *C* and *D*), for which the fitted waist $w_0 \simeq 1\,\mu\mathrm{m}$ for $F_0=0.45$ as compared with $w_0 \simeq 1.3\,\mu\mathrm{m}$ for $F_0=0.35$. The existence of an "optimal" filling factor for superpositions of LG beams is related to the truncation of the highest order (i.e., p value) in the superposition, which is discussed in ref. 36.

Filling Factor Dependence for Trap Frequencies and Dimensions. An important operational issue for bright tweezer trapping of atoms and molecules is confinement near the intensity maxima shown in Fig. 3. From various metrics, here we choose to quantify localization by way of trap vibrational frequencies near the bottom of the trapping potential (i.e., the central intensity maximum for a red-detuned trap), which are modified by pupil apodization and diffraction effects for focused radial LG beams according to their radial mode number p (37).

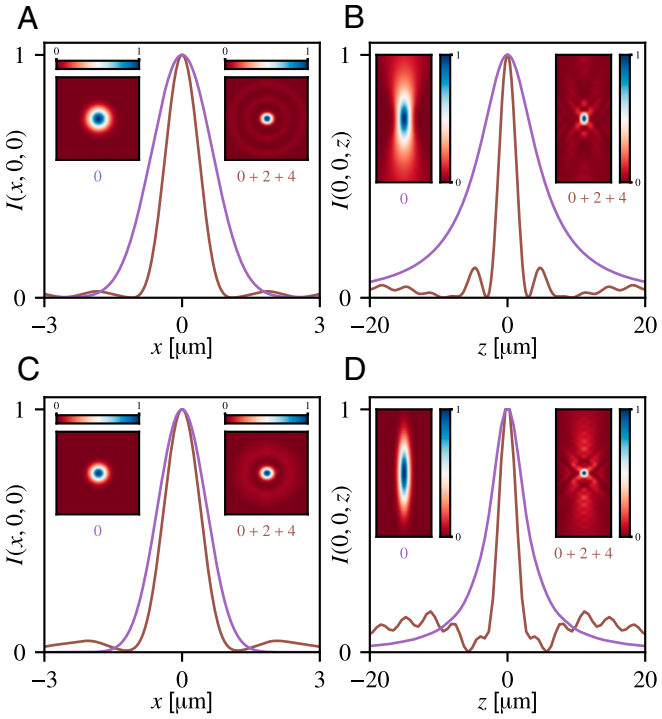

Fig. 3. Focused intensity distributions calculated within the vectorial Debye approximation for x-polarized inputs $\vec{E}_0$ (violet) and $\vec{E}_\Sigma$ (brown). The NA is NA = 0.7, and two filling factor values are compared. (*A*) The x-line cut transverse intensity profiles for $F_0=0.35$. *Left* (right) *Inset* provides the x-y intensity distribution in the focal plane $z=0$ for $\vec{E}_0$ ($\vec{E}_\Sigma$). (*B*) The z-line cut axial intensity profiles for $F_0=0.35$. *Left* (right) *Inset* provides the x-z intensity distribution in the plane $y=0$ for $\vec{E}_0$ ($\vec{E}_\Sigma$). (*C*) Same as *A* for $F_0=0.45$. (*D*) Same as *B* for $F_0=0.45$. Plotted intensities are normalized to their maximum values.

*In the paraxial limit with $l=0$, LG modes are completely specified by wavelength, beam waist, and mode order p, including beam divergence and rms intensity radius, as applied to the source and input fields. However, for wavelength-scale focusing and finite apertures, the full vector theory is required with more complex parametric dependencies.

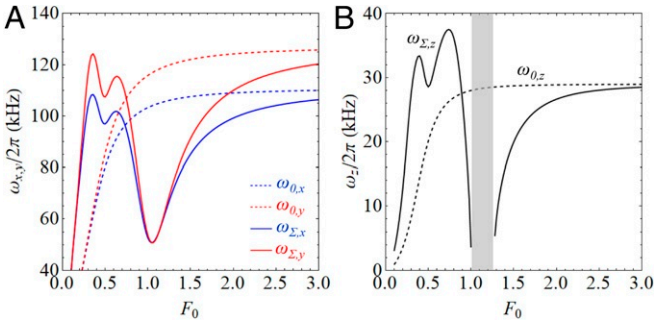

Fig. 4. Radial and axial trap frequencies as a function of filling factor F_0 for the $p=0$ input (dashed) and the 0 + 2 + 4 superposition input (solid; *A*) trap frequencies in *x* (blue) and *y* (red) directions and (*B*) trap frequencies in the *z* direction (black). The gray shaded area represents regions where the trap center becomes a saddle point with a local intensity minimum. All frequencies are evaluated from the trap origin ($x=y=z=0$) with normalized trap depth at $U/k_B=1$ mK.

As an example, we show in Fig. 4 the variation of trap frequency near the trap minimum (intensity maximum) around $x, y, z=0$ for the x-polarized input field distributions $\vec{E}_0$ and $\vec{E}_\Sigma$ as a function of the objective lens filling factor F_0 within the vectorial Debye propagation model (34, 35). The angular trap frequencies ω_x, ω_y, and ω_z are obtained by fitting the trap minimum at $z=0$ to a harmonic potential and extracting the frequency. Fig. 4*A* corresponds to the transverse trap frequencies ω_x and ω_y, while Fig. 4*B* is for the axial frequency ω_z with corresponding intensity distributions for $F_0=0.35$, 0.45 shown in Fig. 3. The gray region in Fig. 4*B* arises when the curvature at $z=0$ becomes antitrapping for $1.0\lesssim F_0\lesssim 1.26$ with the trap minimum located away from the origin. Plots showing the evolution of the trap around these filling factors can be found in *SI Appendix*.

Note that a choice around the local extremum $F_0\sim 0.35$ not only alleviates practical requirements of the objective lens (e.g., focal length and working distance) but also permits focused fields not dominated by diffraction losses. The reduction of both transverse and longitudinal intensity widths for input $\vec{E}_\Sigma$ relative to $\vec{E}_0$ displayed in Fig. 3 is now evident in Fig. 4 for trapping frequencies even in the vector theory with wavelength-scale focusing. For well-chosen filling factors F_0, ω_z for $\vec{E}_\Sigma$ can be larger than any possible value for ω_z achieved with the $\vec{E}_0$ beam (no matter the value of F_0).

Polarization Ellipticity for Tight Focusing. Necessarily, tight focusing of optical fields is accompanied by a longitudinal polarization component, which requires a description beyond the atomic scalar polarizability and which results in spatially dependent elliptical polarization and dephasing mechanisms for atom trapping (38–41). Given the local polarization vector $\hat{\epsilon}$, one can define the vector $\mathbf{C}=\mathrm{Im}(\hat{\epsilon}\times\hat{\epsilon}^*)$, which measures the direction and degree of ellipticity. $|\mathbf{C}|=0$ corresponds to linear polarization, while $|\mathbf{C}|=1$ for circular polarization. Fig. 5*A* provides C_y in the focal plane for the $\vec{E}_\Sigma$ superposition input. Due to tighter confinement, the polarization gradient reaches $dC_y/dx=1.6/\mu\mathrm{m}$ for $\vec{E}_\Sigma$ superposition input, to be compared with $0.4/\mu\mathrm{m}$ for the $p=0$ input $\vec{E}_0$.

We can further quantify the impact of this ellipticity for trapping atoms by the light shifts (scalar, vector, and tensor shifts) of the 0 + 2 + 4 superposition for trapping the Cs atom, as shown in Fig. 5 *B* and *C*. Here, we choose the wavelength at a magic wavelength of Cs ($\lambda=935.7$ nm) with a given trap depth $U/k_B=1$ mK (for $\mathrm{NA}=0.7$ and $F_0=0.35$). Vector light shifts are clearly observed in the transverse direction in Fig. 5*B*. The trap centers for different m_F levels in $6S_{1/2}$, $F=4$ ground state are shifted away from $x=0$ by $\delta x\sim 30$ nm. As the vector light shift is equivalent to a magnetic field gradient along the x direction, it can be suppressed in experiment by an opposite magnetic gradient as demonstrated in ref. 39.

Optimal Filling Factors

As already shown in Fig. 4 and discussed in the previous section, the truncation of LG beams in finite apertures will lead to optimal filling factors for the superposed LG beam input such as the 0 + 2 + 4 superposition. This section focuses on better understanding of this optimization, beginning with Fig. 6*A* (36). Here, we plot the electric field amplitudes for $p=0$, $p=4$ and the 0 + 2 + 4 superposition for filling factor $F_0=0.35$. For $F_0=0.35$, the $p=4$ electric field amplitude (blue curve) is already partially truncated by the aperture (gray area). Further increase of the filling factor will misrepresent the $p=4$ LG beam on the input pupil, and as a result, the foundation of spatial reduction due to Gouy phase superposition will have to be reconsidered. The pupil apodization effects will modify the spatial properties of the focused radial LG beams according to their radial mode number p (37). In fact, larger filling factor truncates the LG beams and can generate completely different field profiles (even bottle beams for a single LG $p=1$ mode input).

Beyond the intuitive picture of truncation of high-order LG beams at larger filling factor, we further developed a simple model based on the analysis of Gouy phase to predict the optimal filling factor (36). For focusing an LG beam with waist $w_{0,\mathrm{in}}$ by a lens with focal length f (assuming the input waist is at the lens position), the ABCD matrix from Gaussian optics predicts the input waist and output waist (w_0) are related by $w_0=f\lambda/\pi w_{0,\mathrm{in}}$. This leads to a Gouy phase as

$$\begin{aligned}\frac{d\psi_G}{dz}&\approx\frac{2p+1}{z_R}\\&=\frac{(2p+1)\pi}{\lambda}\frac{w_{0,\mathrm{in}}^2}{f^2}\\&=\frac{(2p+1)\pi}{\lambda}F_0^2\mathrm{NA}^2.\end{aligned}\qquad[1]$$

In the last step, we use the fact that $F_0=w_{0,\mathrm{in}}/f\mathrm{NA}$. This suggests for a $\mathrm{NA}=1$ system, the phase gradient increases quadratically with F_0 (or input waist $w_{0,\mathrm{in}}$). However, this phase gradient cannot be arbitrarily high for a finite aperture objective. As shown in ref. 36, the maximum phase gradient for an objective with fixed NA is given as

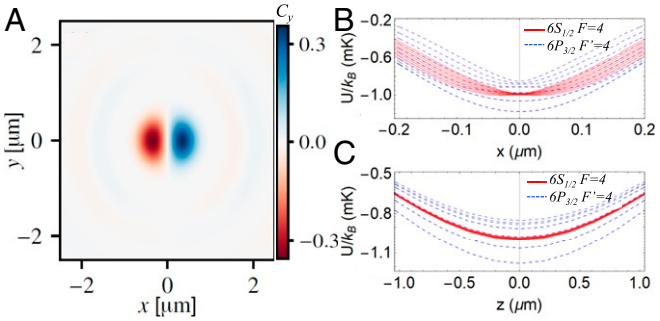

Fig. 5. Polarization ellipticity and vector light shift for the 0 + 2 + 4 input. (*A*) Polarization ellipticity C_y in the focal plane for the 0 + 2 + 4 input with $\mathrm{NA}=0.7$ and $f_0=0.35$. (*B* and *C*) The light shifts for a Cs atom at magic wavelength 935.7 nm with trap depth $U/k_B=1$ mK for transverse (*B*) and axial directions (*C*). The dashed lines indicate the m_F levels in $6S_{1/2}$, $F=4$ ground state (red dashed) and in $6P_{3/2}$, $F'=4$ excited state (blue dashed). In *B*, we can see the ground-state trap is shifted away for the center by $\delta x\sim 30$ nm for the $m_F=4$ sublevel.

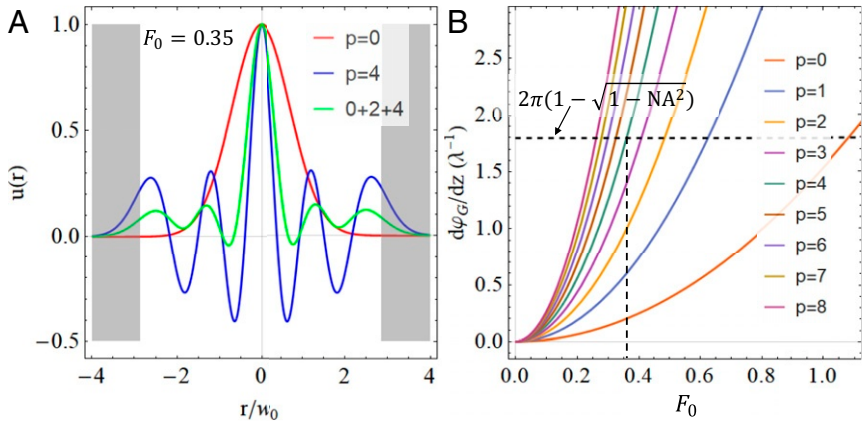

Fig. 6. Interpretation of optimal filling factor F_0 for focusing LG beams with finite aperture objective (36). (*A*) Electric field amplitude of $p = 0$ (red curve), $p = 4$ (blue curve), and 0 + 2 + 4 superposition (green curve) at filling factor $F_0 = 0.35$. The gray shaded region represents the physical cutoff from the entrance pupil of the objective with NA = 0.7. (*B*) Phase gradient of the focused field for different LG beam inputs assuming NA = 1. The horizontal dashed line indicates the maximum available phase gradient from a finite objective with NA = 0.7. The crossing of the horizontal dashed line and phase gradient for $p = 4$ LG beam (green curve) corresponds to a filling factor $F_0 \simeq 0.35$.

$$\left(\frac{d\psi_G}{dz}\right)_{\max} = k(1-\sqrt{1-\mathrm{NA}^2}). \qquad [2]$$

By setting equal the result from Eq. **1** to this maximum phase gradient, we can solve for the optimal filling factor as

$$F_{0,\mathrm{opt}} = \frac{1}{\mathrm{NA}}\left(\frac{2}{2p+1}\right)^{\frac{1}{2}}\left(1-\sqrt{1-\mathrm{NA}^2}\right)^{\frac{1}{2}}. \qquad [3]$$

For NA = 0.7, $p = 4$, this equation predicts an optimal $F_{0,\mathrm{opt}} \simeq 0.36$. In Fig. 6*B*, we show the plot of phase gradient for $p = 0$ to $p = 8$ based on Eq. **1**. The maximum phase gradient for NA = 0.7 is also indicated with the horizontal dashed line. The crossing of NA = 1 phase gradient (colored curves) with the maximum phase gradient for finite aperture predicts the maximum filling factor for each p mode to preserve its property.

Filling Factors and Trap Volumes. We have investigated more globally parameter sets that could provide optimal values for the filling factor F_0, where optimal would be formulated specific to the particular application, such as imaging or reduced scattering in the focal volume as investigated in the next section. In applying optical tweezers for atom trapping, an optimal filling factor might correspond to the highest trap frequency for a given trap depth. It is indeed possible to derive a relation between trap frequency ω and filling factor F_0, at least within the Debye–Wolf formalism, as described in more detail in ref. 36.

Alternatively, for imaging applications, "optimality" might be defined by the value of F_0 that achieves the smallest focal volume for a given NA. Clearly, the focal volumes for both imaging and trapping at the wavelength scale are significantly impacted by diffraction and clipping losses of the input field distributions. To investigate this question, Fig. 7*A* displays volumes V_0 and V_Σ calculated for x-polarized inputs of the fields $\vec{E}_0$ and $\vec{E}_\Sigma$, with details of our operational definition of "volume" given in *SI Appendix*.

Beginning with $F_0 \gg 1$ in Fig. 7*A*, we note that V_0 approaches a lower limit that corresponds to the well-known diffraction-limited point spread function for a uniformly filled objective of NA = 0.7, which is indeed smaller than V_Σ for the field $\vec{E}_\Sigma$ in the same limit $F_0 \gg 1$. However, for more modest values $F_0 \simeq 0.3 - 0.7$, the volume V_0 achieved by $\vec{E}_0$ is significantly larger than V_Σ for $\vec{E}_\Sigma$ if one matches the input waist at the same objective lens entrance for both fields (diagrams of the input fields at the objective entrance for different filling factors can be found in Fig. 7*B* and *SI Appendix*). Moreover, the volume V_Σ achieved for $F_0 = 0.38$ is below even the diffraction limit V_0 for $F_0 \gg 1$. Importantly, the reduced trap volume for V_Σ from $\vec{E}_\Sigma$ derives from improved axial localization along z beyond that achievable with $\vec{E}_0$ for any value of F_0 (*SI Appendix*).

Beyond this general discussion of volume, the behavior of the underlying intensities in the focal volume is complicated for both $\vec{E}_0$ and $\vec{E}_\Sigma$, with the former well documented in textbooks and research literature and the latter much less so. Hence, Fig. 7 *B* and *C* panels display intensity distributions for $\vec{E}_\Sigma$ (Fig. 7*B*) across the source aperture and (Fig. 7*C*) in the focal plane that

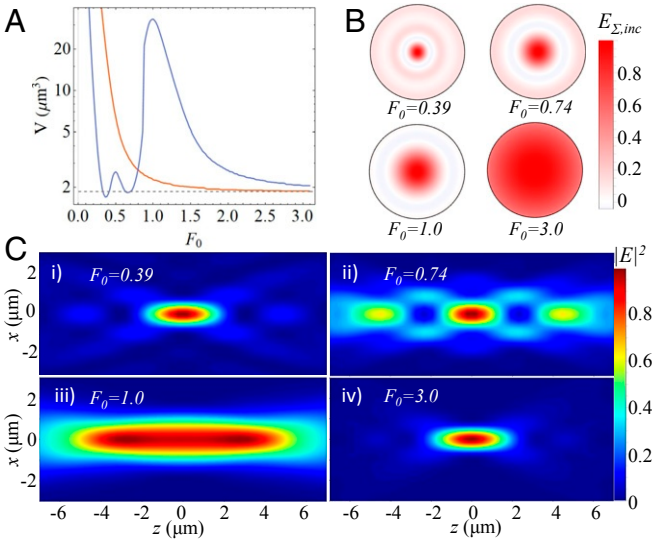

Fig. 7. Trap volumes and focal-plane intensity profiles for a range of filling factors F_0, all with NA = 0.7 (36). (*A*) Trap volume as a function of filling factor for the $p = 0$ input (orange) and the 0 + 2 + 4 superposition input (blue). Here, the trap volume is defined as $V = \Delta x \Delta y \Delta z$, with Δx, Δy, Δz the full widths at half maxima for the intensity distributions along x, y, z. The smallest trap volume we find is $V_\Sigma = 1.7\ \mu\mathrm{m}^3$ at $F_0 = 0.35$. (*B*) The input electric field profile for the 0 + 2 + 4 superposition at filling factors $F_0 = 0.39$, $F_0 = 0.74$, $F_0 = 1$, and $F_0 = 3.0$. (*C*) Intensity profiles near the focus at filling factors $F_0 = 0.39$, $F_0 = 0.74$, $F_0 = 1$, and $F_0 = 3$. Note that the airy rings observed in *i–iii* are still present in *iv*, although not revealed due to their small size and the limited contrast.

are much more complicated than those for E_0 and which exhibit structure in regions well outside the central maxima (including strong side lobes and extended axial variations) (*SI Appendix*). Such side lobes can introduce atom heating for transport of cold atoms in moving tweezers, thereby reducing atom delivery efficiency from free space to dielectric surfaces. Two other filling factors $F_0 = 1$ and $F_0 = 3$ are also presented in Fig. 7 *B* and *C*. Note that $F_0 = 1$ in Fig. 7 *C*, *iii* corresponds to a flattened trap intensity in the axial direction with properties similar to Bessel beams (42), with plots of this effect and discussion found in *SI Appendix*. Finally, $F_0 = 3$ in Fig. 7 *C*, *iv* approaches the limit of a uniform input with a well-known diffraction-limited spot size.

While we have considered here two examples of optimization by way of trapping frequencies and volumes in tweezer traps, similar analyses can be formulated to optimize other metrics (36). Indeed, the systematic search for optimal values of F_0 briefly described in this section immediately found the peaks shown in Fig. 4 for atom trapping, which we first identified by a considerably more painful random search. Moreover, because trap volumes for focused red traps scale as $V_{\text{trap}} \propto (\omega_z \omega_x \omega_y)^{-1}$, the expressions for trap frequencies in the axial and transverse directions can be combined to find optimal filling factors F_0 to minimize trap volume around the center of a trap for a given input profile E_{in} for comparison with more global measures of volume (e.g., FWHM) (*SI Appendix*).

LG Beams Reflected from Dielectric Nanostructures

Excepting Fig. 1*D*, we have thus far directed attention to free-space optical tweezers for atoms and molecules. However, there are important settings for both particle trapping and imaging in which the focal region is not homogeneous but instead, contains significant spatial variations of the dielectric constant over a wide range of length scales from nanometers to micrometers. Important examples in atomic, molecular, and optical (AMO) physics include recent efforts to trap atoms near nanophotonic structures such as dielectric optical cavities and photonic crystal waveguides (PCWs) (26, 39, 43–46). These efforts have been hampered by large modification of the trapping potential of an optical tweezer in the vicinity of a nanophotonic structure, principally associated with specular reflection that produces high-contrast interference fringes extending well beyond the volume of the tweezer.

The magnitude of the problem is already made clear in the paraxial limit by the blue curve in Fig. 1*D*. The otherwise smoothly varying tweezer intensities in free space, shown in Fig. 1 *A* and *B*, become strongly modulated in Fig. 1*D* by the reflection of the tweezer field from the dielectric surface. Given that the goal for the integration of cold atoms and nanophotonics is to achieve one-dimensional (1D) and two-dimensional (2D) atomic lattices trapped at distances $z \lesssim \lambda/10$ from surfaces and that one interference fringe in Fig. 1 spans $\Delta z = \lambda/2$, it is clear that free-space tweezer traps cannot be readily employed for direct transport of atoms along a linear trajectory in z to the near fields of nanoscale dielectrics without implementing more complicated trajectories. These trajectories not only require the tweezer spot to traverse along z but x or y as well (47). Further insight for direct transport along z is provided by the animations in *SI Appendix* for the evolution of the intensity of a conventional optical tweezer as the focal spot is moved from an initial distance $z_i \gg \lambda$ to a final distance $z_0 = 0$ at the dielectric surface. Placing atoms at distances $z \lesssim \lambda/10$ from dielectric surfaces is possible by combining LG beam optical tweezers and utilizing guided modes (GMs) of the dielectric structure. These GMs can be configured in such a way to attract the atoms via the dipole force to stable trapping regions $z \lesssim \lambda/10$ from the dielectric. Such trapping configurations are discussed in ref. 45.

That said, Fig. 1*D* investigates a strategy to mitigate this difficulty by exploiting the rapid spatial variation of the Gouy phase Ψ_Σ for the field $\vec{E}_\Sigma$ as compared with Ψ_0 for the field $\vec{E}_0$. As shown by the orange curve in Fig. 1*D*, the contrast and spatial extent of near-field interference are greatly reduced for $\vec{E}_\Sigma$ due to rapid spatial dephasing between input and reflected fields.

To transition this idea into the regime of nanophotonic structures with tightly focused tweezer fields on the wavelength scale, we start with a free-space LG beam in the paraxial limit with waist much larger than the optical wavelength, $w_0 \gg \lambda$. The optical field for this initial LG beam is first "sculpted" with the SLM and then tightly focused as in Fig. 2 with fields in the free-space focal volume calculated from the Debye–Wolf formalism and serving as a background field without scattering. We then solve for the scattered field in the presence of a dielectric nanostructure in the focal volume.

An example to validate directly the possibility of reduced reflection and "fringe" fields for wavelength-scale optical

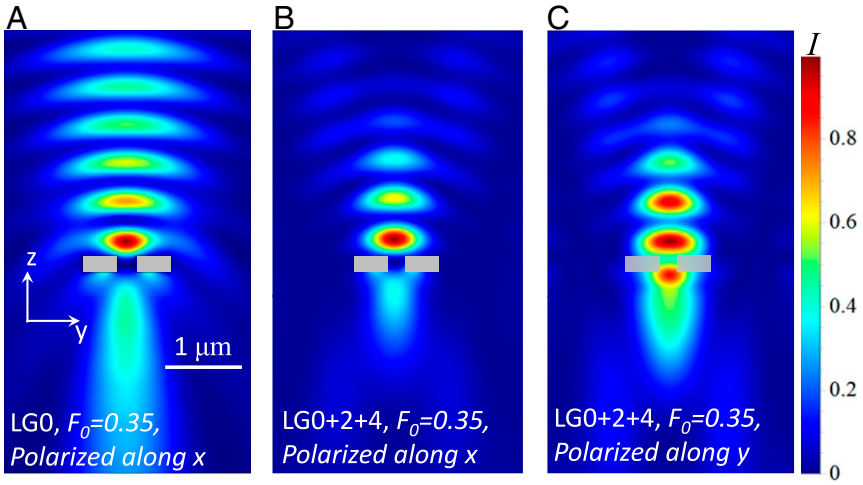

Fig. 8. Simulation of aligning a tightly focused LG beam to reflect and scatter from an APCW directed out of the page (indicated by the gray rectangles) with focal position aligned to the geometric center of the APCW (*A*) for the input field distribution of a $p = 0$ Gaussian beam with initial polarization along *x*, (*B*) for the input field distribution of the 0 + 2 + 4 superposed LG beam with polarization along *x*, and (*C*) for the input field distribution of the 0 + 2 + 4 superposed LG beam with polarization along y. All three plots are calculated with the background field derived from the Debye–Wolf integral with NA = 0.7 and $F_0 = 0.35$ (36).

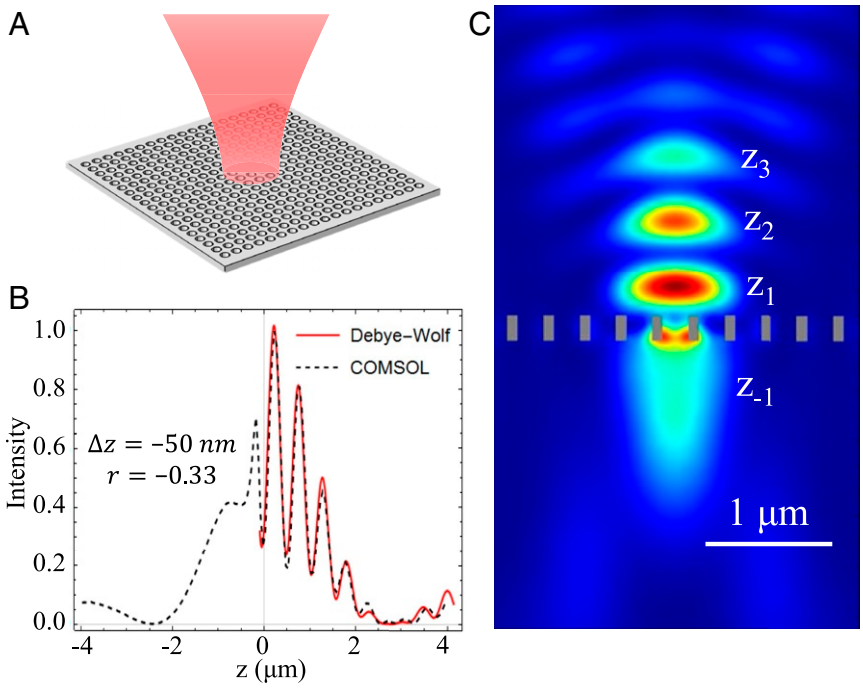

Fig. 9. (*A*) Optical tweezer focused on a 2D photonic crystal slab. (*B*) Fitting of the Comsol simulated field (dashed line) with the Debye–Wolf evaluated field reflecting from a planar surface (red solid line). (*C*) The Comsol simulated field of the LG 0 + 2 + 4 superposition E_Σ reflected from a 2D PCW that is composed of a dielectric slab with a 2D square lattice of holes as in ref. 49.

tweezers near nanophotonic devices is presented in Fig. 8, which displays intensity distributions calculated for (Fig. 8*A*) a focused $p = 0$ Gaussian beam input and (Fig. 8 *B* and *C*) a focused 0 + 2 + 4 superposed LG beam aligned to an alligator photonic crystal waveguide (APCW) (48) for NA = 0.7 and $F_0 = 0.35$. This result confirms the spatial reduction of fringe fields from the superposition of LG beams near complex dielectric nanostructures.

We stress that our methods for finding the reflected and scattered fields for nanophotonic devices illuminated by coherent sums of LG fields can be readily extended from 1D to 2D slab PCWs (49, 50). One such result for a 2D square lattice (49) has been calculated with the vector theory and is displayed in Fig. 9, again with reduced reflected fields brought by interference from the range of Gouy phases.

Atom Transport to a Photonic Crystal

To investigate the efficiency for atom transport from free-space optical tweezers to reflective traps near dielectric surfaces, we have performed Monte Carlo simulations of atom trajectories by

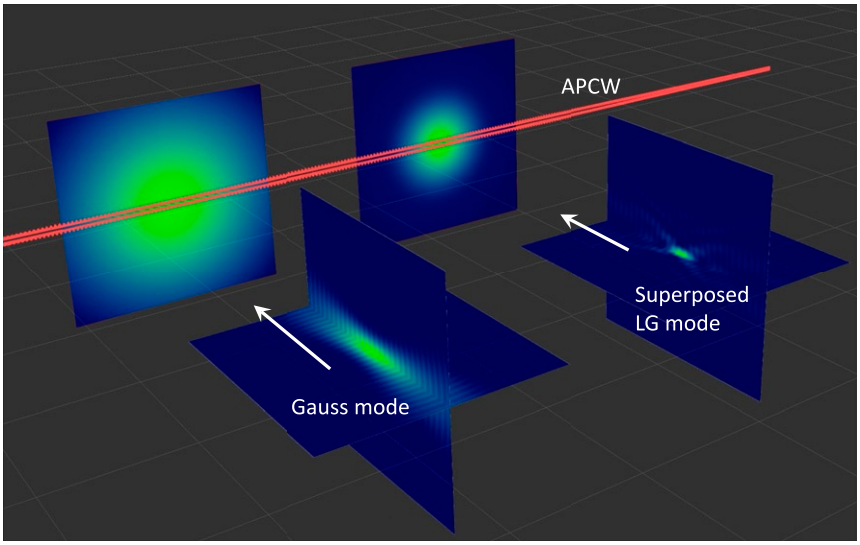

Fig. 10. Single frame from an animation of atom delivery to the APCW (in red) by way of a moving optical tweezer. (*Left*) Gaussian beam E_0. (*Right*) Coherent superposition of LG beams $\vec{E}_\Sigma$. In the displayed frame, atoms are absent to better highlight the intensity distributions of the two optical tweezers. The white arrows indicate the direction of motion of the tweezer focus as implemented in refs. 51 and 52, and the grids are 10 × 10 μm. The full animation depicts noninteracting atoms as white "dots" as might have been initially loaded and cooled into the tweezers far from the APCW (20 atoms for each tweezer). A movie can be found at the following link: https://data.caltech.edu/records/1446.

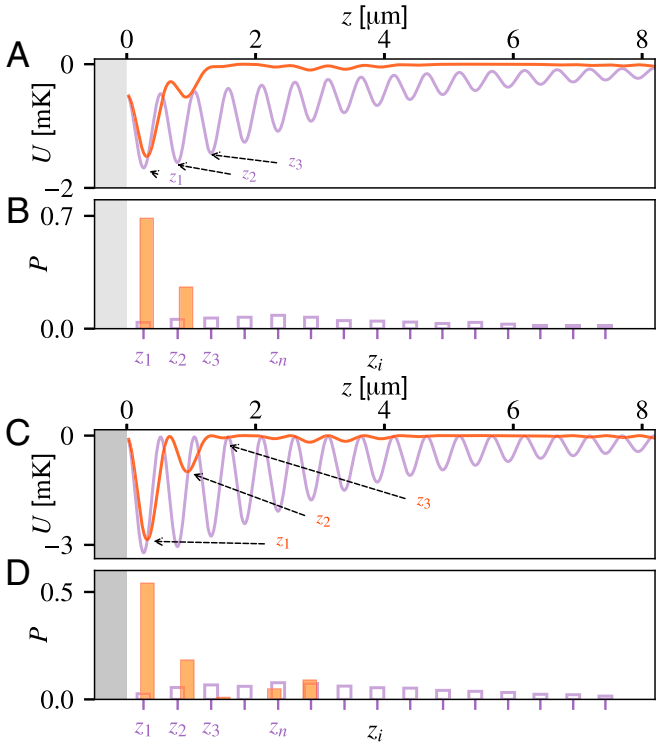

Fig. 11. Results from Monte Carlo simulation of cold-atom delivery close to a semiinfinite planar surface with an amplitude reflection coefficient $r = -0.3$ for *A* and *B* and $r = -0.8$ for *C* and *D*. (*A* and *C*) Optical potentials $U(0, 0, z)$ for optical tweezers formed from the fields $\vec{E}_0$ (violet) and $\vec{E}_\Sigma$ (orange), respectively, as in Fig. 1*D* for focus at $z = 0$. (*B* and *D*) The final probabilities $P(z_i)$ for delivery of atoms to optical traps centered at positions z_i. Atoms are initially loaded into an optical tweezer of depth $U_0 = 1$ mK at focal distance $z_{initial} = 600$ μm from the surface and initial temperature of 100 μK. The focal plane of the optical tweezer is then scanned from $z_{initial}$ to $z_{final} = 0$ μm. z_n indicates the optical trap formed from $\vec{E}_0$ with highest delivery probability. Full numerical simulations of atom transport can be found in *SI Appendix* and provide the basis for this figure.

moving a tweezer's focus position from far away ($z = 600$ μm) to the surfaces ($z = 0$ μm) of various nanophotonic devices. These simulations have been carried out for both the paraxial regime and with the full vector theory of Debye–Wolf.

Fig. 10 and the accompanying animation provide a global view of the intensity for an optical tweezer whose focus is initially located far from the APCW then moved to the surface of the APCW. Two tweezer fields are shown, first for the field $\vec{E}_0$ for a conventional $p = 0$ Gaussian tweezer and second for the unconventional field $\vec{E}_\Sigma$ for the coherent superposition of $p = 0, 2, 4$ beams.

With the overall view in mind from the animation accompanying Fig. 10, we finally address the question of quantitatively assessing the efficiency of atom transport from free-space tweezers to the near fields of nanophotonic structures for optical tweezers with E_Σ compared with tweezers with E_0. Fig. 11 provides such an assessment of the probabilities for single atoms to be delivered and trapped in surface traps of a reflecting dielectric. The specific choice of reflection coefficient $r = -0.8$ is based on numerical simulations of wavelength-scale tweezer reflection from the nanoscale surface of an APCW for polarization parallel (44) to the long axis of the APCW.

Fig. 11*B* confirms that the trap formed by the superposition $\vec{E}_\Sigma$ (orange histogram) leads to large enhancement in delivery efficiency into near-surface traps (z_1, z_2...) as compared with the very small probability of delivery for the conventional trap formed by $\vec{E}_0$ (violet histogram). The probability of delivering an atom into the z_1 trap with $\vec{E}_\Sigma$ is $P_\Sigma(z_1) \simeq 0.55$ as compared with $P_0(z_1) \simeq 0.03$ with $\vec{E}_0$. Fig. 11 is from a 1D model of atom transport [i.e., in the optical potential $U(0, 0, z)$] and hence, provides only a qualitative guide. We have also carried out full 3D simulations for the situation of Fig. 1*D*, with comparable results [e.g., $P_\Sigma(z_1) \simeq 0.45$] presented in *SI Appendix*.

Moreover, beyond the protocols considered in Fig. 11 and in *SI Appendix*, we have found improvements in delivery efficiency by including atom cooling in the simulations at various stages of the transport, as well as applying blue-detuned GM beams as atoms arrive near the surface to overcome loss due to surface forces such as the Casimir–Polder potential. Finally, to document the robustness of our scheme, results from simulations analogous to those in Fig. 11 are presented in *SI Appendix* for $r = -0.3$ corresponding to an optical tweezer with polarization perpendicular to the long axis of an APCW, for which $P_\Sigma(z_1) \simeq 0.68$.

Conclusion and Outlook

We have proposed coherent superpositions of radial LG beams for bright optical tweezers. By way of a vector theory that encompasses diffraction and tight focusing on the wavelength scale, we have investigated possibilities for reduced trap volumes and increased trapping frequencies for free-space tweezer traps constrained by fixed NA. A specific application has been numerically analyzed for the efficient transport of atoms via red-detuned optical tweezers directly to trap sites near the surfaces of nanoscopic dielectric structures. The key feature of our approach is the suppression of interference fringes from reflection near nanoscopic dielectric surfaces. Our goal is to enable a leap forward for cold-atom delivery and manipulation to allow the assembly of 1D and 2D nanoscopic atomic lattices near PCWs by way of the optical tweezers that we describe. While bits and pieces of our protocols have appeared in prior papers, to our knowledge, the key aspects of the results presented in our manuscript have not been known heretofore.

Beyond atom trapping with optical tweezers in AMO physics, we are currently exploring imaging techniques with large phase gradients and subwavelength-scale resolution. For example, Fig. 10 and the accompanying animation document the potential for significantly reduced depth of field (and hence, possible improved axial resolution) for illumination and detection by way of coherent superpositions of LG beams, specifically the field $\vec{E}_\Sigma$ relative to the conventional field $\vec{E}_0$.

More generally, the possibility to engineer Gouy phase shifts for sums of tightly focused radial LG fields might extend the range of imaging methods to permit phase-contrast microscopy strategies on a subwavelength scale, which is an application that we are currently exploring. Beyond engineered nanophotonic structures, the suppression or enhancement of interference from diffuse reflection and scattering in spatially heterogeneous sample volumes (e.g., living cells) is another application under consideration.

Data Availability. This article contains no measured data associated with the theoretical results presented, excepting preliminary measurements shown in Figs. S7 and S8 in the Supporting Information (SI) for which the data are clearly displayed. Numerical results calculated from the underlying theory of the article and SI are deposited in a publicly available archive (The Caltech Research Data Repository https://data.caltech.edu/), with specific links given in the main article and SI. Further information is available from the lead author J-.B.B. upon request to jbbeguin@caltech.edu.

ACKNOWLEDGMENTS. We thank Robert Boyd and Nick Black for discussions related to SLMs. J.L. acknowledges funding from the French–US Fulbright Commission, French National Research Agency NanoStrong Project ANR-18-CE47-0008, and Région Ile-de-France (DIM SIRTEQ). H.J.K.

acknowledges funding from Office of Naval Research (ONR) Multidisciplinary University Research Initiative (MURI) Quantum Opto-Mechanics with Atoms and Nanostructured Diamond Grant N000141512761, ONR Grant N000141612399, Air Force Office of Scientific Research (AFOSR) MURI Photonic Quantum Matter Grant FA95501610323, NSF Grant PHY1205729, and Caltech Kavli Nanoscience Institute (KNI).

1. L. Allen, S. M. Barnett, M. J. Padgett, *Optical Angular Momentum* (IOP Publishing, 2003).
2. A. Ashkin, *Optical Trapping and Manipulation of Neutral Particles Using Lasers* (World Scientific, 2006).
3. D. G. Grier, A revolution in optical manipulation. *Nature* **424**, 810–816 (2003).
4. Q. Zhan, Cylindrical vector beams: From mathematical concepts to applications. *Adv. Opt. Photon.* **1**, 1–57 (2009).
5. R. Dorn, S. Quabis, G. Leuchs, Sharper focus for a radially polarized light beam. *Phys. Rev. Lett.* **91**, 233901 (2003).
6. H. Wang, L. Shi, B. Lukyanchuk, C. Sheppard, C. T. Chong, Creation of a needle of longitudinally polarized light in vacuum using binary optics. *Nat. Photon.* **2**, 501–505 (2008).
7. P. Wońiak *et al.*, Tighter spots of light with superposed orbital-angular-momentum beams. *Phys. Rev.* **94**, 021803 (2016).
8. M. Padgett, R. Bowman, Tweezers with a twist. *Nat. Photon.* **5**, 343–348 (2011).
9. S. Franke-Arnold, Optical angular momentum and atoms. *Phil. Trans. A Math. Phys. Eng. Sci.* **375**, 20150435 (2017).
10. M. Babiker, D. L. Andrews, V. E. Lembessis, Atoms in complex twisted light. *J. Opt*. **21**, 013001 (2018).
11. T. Kuga *et al.*, Novel optical trap of atoms with a doughnut beam. *Phys. Rev. Lett.* **78**, 4713–4716 (1997).
12. J. L. Chaloupka, Y. Fisher, T. J. Kessler, D. D. Meyerhofer, Single-beam, ponderomotive-optical trap for free electrons and neutral atoms. *Opt. Lett.* **22**, 1021–1023 (1997).
13. R. Ozeri, L. Khaykovich, N. Davidson, Long spin relaxation times in a single-beam blue-detuned optical trap. *Phys. Rev.* **59**, R1750–R1753 (1999).
14. J. Arlt, M. J. Padgett, Generation of a beam with a dark focus surrounded by regions of higher intensity: The optical bottle beam. *Opt. Lett.* **25**, 191–193 (2000).
15. A. S. Arnold, Extending dark optical trapping geometries. *Opt. Lett.* **37**, 2505–2507 (2012).
16. P. Xu, X. He, J. Wang, M. Zhan, Trapping a single atom in a blue detuned optical bottle beam trap. *Opt. Lett.* **35**, 2164–2166 (2010).
17. D. Barredo *et al.*, Three-dimensional trapping of individual Rydberg atoms in ponderomotive bottle beam traps. *Phys. Rev. Lett.* **124**, 023201 (2020).
18. S. Hell, E. H. K. Stelzer, Properties of a 4pi confocal fluorescence microscope. *J. Opt. Soc. Am. A* **9**, 2159–2166 (1992).
19. N. Bokor, N. Davidson, Toward a spherical spot distribution with 4π focusing of radially polarized light. *Opt. Lett.* **29**, 1968–1970 (2004).
20. R. W. Boyd, Intuitive explanation of the phase anomaly of focused light beams. *J. Opt. Soc. Am.* **70**, 877 (1980).
21. O. Steuernagel, E. Yao, K. O'Holleran, M. Padgett, Observation of Gouy-phase-induced transversal intensity changes in focused beams. *J. Mod. Opt*. **52**, 2713–2721 (2005).
22. T. Birr *et al.*, Phase-resolved observation of the Gouy phase shift of surface plasmon polaritons. *ACS Photonics* **4**, 905–908 (2017).
23. L. Isenhower, W. Williams, A. Dally, M. Saffman, Atom trapping in an interferometrically generated bottle beam trap. *Opt. Lett.* **34**, 1159–1161 (2009).
24. A. Whiting, A. Abouraddy, B. Saleh, M. Teich, J. Fourkas, Polarization-assisted transverse and axial optical superresolution. *Optics Express* **11**, 1714–1723 (2003).
25. T. Freegarde, K. Dholakia, Cavity-enhanced optical bottle beam as a mechanical amplifier. *Phys. Rev.* **66**, 013413 (2002).
26. D. E. Chang, J. S. Douglas, A. González-Tudela, C. L. Hung, H. J. Kimble, Colloquium: Quantum matter built from nanoscopic lattices of atoms and photons. *Rev. Mod. Phys.* **90**, 031002 (2018).
27. L. Allen, M. W. Beijersbergen, R. J. C. Spreeuw, J. P. Woerdman, Orbital angular momentum of light and the transformation of Laguerre-Gaussian laser modes. *Phys. Rev. A* **45**, 8185–8189 (1992).
28. A. E. Siegman, *Lasers* (Oxford University, Oxford, United Kingdom, 1986).
29. R. L. Phillips, L. C. Andrews, Spot size and divergence for Laguerre Gaussian beams of any order. *Appl. Opt.* **22**, 643–644 (1983).
30. T. Ando, Y. Ohtake, N. Matsumoto, T. Inoue, N. Fukuchi, Mode purities of Laguerre-Gaussian beams generated via complex-amplitude modulation using phase-only spatial light modulators. *Opt. Lett.* **34**, 34–36 (2009).
31. J. Arlt, K. Dholakia, L. Allen, M. J. Padgett, The production of multiringed laguerre-Gaussian modes by computer-generated holograms. *J. Mod. Opt.* **45**, 1231–1237 (1998).
32. J. A. Davis, D. M. Cottrell, J. Campos, M. J. Yzuel, I. Moreno, Encoding amplitude information onto phase-only filters. *Appl. Opt.* **38**, 5004–5013 (1999).
33. E. Bolduc, N. Bent, E. Santamato, E. Karimi, R. W. Boyd, Exact solution to simultaneous intensity and phase encryption with a single phase-only hologram. *Opt. Lett.* **38**, 3546–3549 (2013).
34. B. Richards, E. Wolf, Electromagnetic diffraction in optical systems, ii. Structure of the image field in an aplanatic system. *Proc. R. Soc. Lond. A Math. Phys. Sci.* **253**, 358–379 (1959).
35. L. Novotny, B. Hecht, *Principles of Nano-Optics* (Cambridge University Press, Cambridge, United Kingdom, 2006).
36. X. Luan, "Towards atom assembly on nanophotonic structures with optical tweezers," PhD thesis, California Institute of Technology, Pasadena, CA (2020).
37. S. Haddadi, D. Louhibi, A. Hasnaoui, A. Harfouche, K. Aït-Ameur, Spatial properties of a diffracted high-order radial Laguerre-Gauss LG_{p0} beam. *Laser Phys.* **25**, 125002 (2015).
38. S. Kuhr *et al.*, Analysis of dephasing mechanisms in a standing-wave dipole trap. *Phys. Rev. A* **72**, 023406 (2005).
39. J. D. Thompson, T. G. Tiecke, A. S. Zibrov, V. Vuletić, M. D. Lukin, Coherence and Raman sideband cooling of a single atom in an optical tweezer. *Phys. Rev. Lett.* **110**, 133001 (2013).
40. A. Goban *et al.*, Demonstration of a state-insensitive, compensated nanofiber trap. *Phys. Rev. Lett.* **109**, 033603 (2012).
41. D. Hümmer, P. Schneeweiss, A. Rauschenbeutel, O. Romero-Isart, Heating in nanophotonic traps for cold atoms. *Phys. Rev. X* **9**, 041034 (2019).
42. J. Durnin, J. J. Miceli, J. H. Eberly, Diffraction-free beams. *Phys. Rev. Lett.* **58**, 1499–1501 (1987).
43. T. Tiecke *et al.*, Nanophotonic quantum phase switch with a single atom. *Nature* **508**, 241–244 (2014).
44. J. D. Hood *et al.*, Atom–atom interactions around the band edge of a photonic crystal waveguide. *Proc. Natl. Acad. Sci. U.S.A.* **113**, 10507–10512 (2016).
45. A. P. Burgers *et al.*, Clocked atom delivery to a photonic crystal waveguide. *Proc. Natl. Acad. Sci. U.S.A.* **116**, 456–465 (2019).
46. M. E. Kim, T. H. Chang, B. M. Fields, C. A. Chen, C. L. Hung, Trapping single atoms on a nanophotonic circuit with configurable tweezer lattices. *Nat. Commun.* **10**, 1647 (2019).
47. J. D. Thompson *et al.*, Coupling a single trapped atom to a nanoscale optical cavity. *Science* **340**, 1202–1205 (2013).
48. S. P. Yu *et al.*, Nanowire photonic crystal waveguides for single-atom trapping and strong light-matter interactions. *Appl. Phys. Lett.* **104**, 111103 (2014).
49. S. P. Yu, J. A. Muniz, C. L. Hung, H. J. Kimble, Two-dimensional photonic crystals for engineering atom-light interactions. *Proc. Natl. Acad. Sci. U.S.A.* **116**, 12743–12751 (2019).
50. A. González-Tudela, C. L. Hung, D. E. Chang, J. I. Cirac, H. J. Kimble, Subwavelength vacuum lattices and atom-atom interactions in two-dimensional photonic crystals. *Nat. Photon.* **9**, 320–325 (2015).
51. J. B. Béguin *et al.*, Advanced apparatus for the integration of nanophotonics and cold atoms. *Optica* **7**, 1–2 (2020).
52. X. Luan *et al.*, The integration of photonic crystal waveguides with atom arrays in optical tweezers. *Adv. Quantum Technol.*, 10.1002/qute.202000008 (2020).